JAAS

Cite this: *J. Anal. At. Spectrom.*, 2012, **27**, 390

www.rsc.org/jaas

PAPER

In-depth multi-technique characterization of chromium–silicon mixed oxides produced by reactive ion beam mixing of the Cr/Si interface

R. Escobar Galindo,*[a] N. Benito,[b] D. Duday,[c] G. G. Fuentes,[d] N. Valle,[c] P. Herrero,[a] L. Vergara,[a] V. Joco,[e] O. Sanchez,[a] A. Arranz[b] and C. Palacio[b]

Received 4th October 2011, Accepted 21st December 2011
DOI: 10.1039/c2ja10296j

The great interest of mixed metal–silicon oxides lies in their suitability, among other applications, as optical coatings with an adjustable refractive index. In this paper we investigate a new method to obtain chromium and silicon mixed oxides. Using as starting point a metallic chromium film deposited on a silicon substrate by magnetron sputtering, we induce the formation of mixed oxides using reactive ion beam mixing by bombarding the Cr/Si interface with oxygen. We have varied the ion fluence (between 5×10^{16} and 1×10^{18} ions cm^{-2}) at a fixed implantation energy of 80 keV in order to modify the final composition of the coating. The composition profiles have been obtained with Rutherford backscattering spectroscopy (RBS), by changing the He energy from 3.035 up to 3.105 MeV, and with elastic recoil detection analysis using a time of flight configuration (ERDA-ToF). Results have been compared with those obtained from secondary ion mass spectrometry (SIMS) depth profiles and Monte Carlo TRIDYN simulations. Concentration depth profiles (CDP) have been also measured using X-ray photoelectron spectroscopy (XPS) and simultaneous Ar^+ bombardment, as well as angle-resolved X-ray photoelectron spectroscopy (ARXPS). All the obtained depth profiles agree remarkably well with cross-section transmission electron microscopy (TEM) observations made on the sample implanted at the highest fluence.

Introduction

The use of mixed oxides to improve the performance of simple binary oxides has been extensively applied in different technological niches. In photocatalytic applications, titanium dioxide films have been doped with other metals (Zr, W, and Mo) in order to prevent the anatase-to-rutile phase transformation and, therefore, shift the absorption threshold towards the visible range.[1–5] In electronics, ternary oxides like Zr–Si–O or Hf–Zr–O have been suggested as high-*k* gate oxides to substitute silicon dioxide in complementary metal–oxide-semiconductors (CMOS) as they can work at lower equivalent oxide thicknesses (EOT) and smaller interface state densities than the binary oxide.[6,7] Al–Ti–O, Ti–Si–O and Cr–Si–O mixed oxides have also been proposed for applications in optics as materials with a variable refractive index.[8,9] Other applications of the mixed oxides can be found in the catalysis and the electrochromic sectors.[10–12] On top of these specific properties, the use of mixed oxides can also improve the corrosion and wear resistance at high temperatures of the final device. It is evident that the optimization of these properties can only be obtained through a severe control of the synthesis process, including a proper choice of materials, deposition technique, composition, morphology, thermal stability or interface reactivity, to name just a few.

Chemical vapour deposition (CVD) based techniques, mainly plasma enhanced and ion beam induced CVD (PECVD and IBICVD, respectively), are commonly used to produce mixed oxides.[8] However, the use of metalorganics as gas precursors may provoke the incorporation of chlorine, hydrogen or carboxyl groups into the deposited films and a subsequent deterioration of the optical and electronic properties, as well as the occurrence of corrosion at high temperature conditions. Moreover, it is quite difficult to synthesize ternary oxides by CVD because of the need of precursor mixtures or complex bimetallic precursors that hinder the control of the film stoichiometry. Therefore, alternative synthesis processes should be addressed. Reactive magnetron sputtering is a promising candidate, since mixed oxides can be obtained by controlling the deposition parameters (cathode composition, applied power, energy of the ions present in the plasma, *etc.*) and since it is an easily industrially scalable technique that allows the deposition of films with thickness above 1000 nm within reasonable process times. Moreover,

[a]*Instituto Ciencia Materiales de Madrid, ICMM-CSIC, 28049 Madrid, Spain. E-mail: rescobar@icmm.csic.es; Fax: +34 91 372 0623; Tel: +34 91 334 9000*
[b]*Departamento de Física Aplicada, Universidad Autónoma de Madrid, 28049 Madrid, Spain*
[c]*Centre de Recherche Public—Gabriel Lippmann, 4422 Belvaux, Luxembourg*
[d]*AIN, Centro de Ingeniería Avanzada de Superficies, 31191 Cordovilla, Pamplona, Spain*
[e]*Centro de Micro-análisis de Materiales, 28049 Madrid, Spain*

This journal is © The Royal Society of Chemistry 2012

Vergara *et al.*[13] and Benito *et al.*[14] have recently shown the viability of reactive magnetron sputtering to the control of the optical properties of silicon and chromium mixed oxides. A second alternative synthesis is ion beam mixing (IBM), where compounds are formed by bilayer mixing using ion beams.[15] IBM is a feasible technique to form new phases otherwise impossible to be produced using the above-mentioned conventional techniques.[16] One of the advantages of IBM is that it allows a fundamental study on the interface reaction at different thickness scales by changing the ion beam energy. Fig. 1 depicts a schematic representation of the IBM process. During the irradiation of the bilayer structure, ions provide locally high energy, which induces a strong atomic diffusion leading to interface mixing and chemical reactions. IBM has been successfully applied to the formation of metal silicides using inert argon bombardment at the Cr/Si and Ti/Si interfaces,[16,17] and of mixed nitride systems using nitrogen ion beams.[18–20] Although the implantation of oxygen has been applied to the study of the formation of MeO_x binary systems,[21,22] IBM has never been employed as a route to obtain mixed oxides, to our knowledge.[23]

The main objective of this work is to assess the potential use of IBM to obtain mixed Cr–Si oxide thin films whose properties can be tuned between those of each of the constituent binary oxides so as to use them as films with a variable refractive index for functional and/or structural applications. In particular, we have performed an extensive multi-technique depth profile characterisation of the implanted films by means of Rutherford backscattering spectroscopy (RBS), elastic recoil detection analysis using a time of flight configuration (ERDA-ToF), secondary ion mass spectrometry (SIMS), X-ray photoelectron spectroscopy (XPS) and transmission electron microscopy (TEM), and compared the results with Monte Carlo TRIDYN simulations.

Experimental

Prior to the physical deposition and implantation of the samples and to get further insight, the reactive IBM of Cr/Si interfaces has been simulated using the dynamic Monte Carlo TRIDYN code (version 4.0).[24,25] TRIDYN treats the atomic interactions as a sequence of binary collisions between atoms using a screened Coulomb potential with the WHB (Kr–C) screening function.[26,27] For the electronic energy loss, an equipartition of the Lindhard and Scharff and the Oen and Robinson models is used.[26,28,29] The heat of sublimation has been used for the chromium and silicon surface binding energies (4.1 and 4.7 eV, respectively), whereas

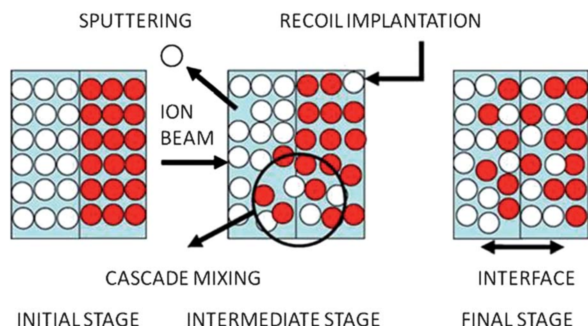

Fig. 1 Schematic representation of the ion beam mixing process.

for oxygen, it has been estimated to be ~6.9 eV.[30] The bulk binding energies have been set to zero,[30] while the maximum oxygen concentration has been limited to 66 at.%. With the TRIDYN routine, not only the dynamic change of the thickness and composition of the target substrate during reactive IBM is accounted for, but so are the changes in the chromium, silicon and oxygen sputtering yields, preferential sputtering, and pure ballistic atomic mixing mechanisms.

Metallic chromium layers were deposited on a 3-inch silicon (100) wafer by DC magnetron sputtering in a high-purity (99.999%) argon atmosphere. The sputtering chamber was pumped down to a base pressure below 8.6×10^{-6} mbar before letting in the gas (11 sccm Ar). Prior to the deposition, the 3-inch chromium target was sputtered for 10 minutes in order to clean its surface, while covering the substrates with a shutter. The substrate holder, placed at a distance of 12 cm from the target, was electrically isolated, with no bias voltage applied externally. Likewise, no intentional heating of the substrates was performed during deposition. A sputtering time of 7 minutes for a DC power of 100 W led to a film thickness of 95 ± 3 nm, determined both with a Veeco Dektak 150 stylus surface profiler by measuring the height of a step left by a mechanical mask, and by cross-sectional scanning electron microscopy (SEM) observation by means of an INCAx-sight FE-SEM with a resolution of 136 eV when operating at 5.9 keV. X-Ray diffraction on the as-deposited samples (not shown in this paper) assessed that the films were polycrystalline metallic chromium with (110) and (200) orientations. The silicon wafer with the chromium layer deposited on top was afterwards cut in 2×2 cm^2 pieces to be used in the different implantation procedures.

Oxygen implantation was performed in a Whickham Ion Beam System 200 high-current implanter.[31] The setup is equipped with a Freeman ion source able to produce ion beams of most of elements, and a mass analyser magnet to separate all isotopes from hydrogen to lead. The maximum implantation energy is 200 keV for singly charged ions, while the maximum ion currents are up to 0.1–0.3 mA cm^{-2} for O^+. The size of the ion beam is 2–3 cm^2. Stopping and range of ions in matter (SRIM) simulations were performed in order to adjust the oxygen implantation range to the thickness of the metallic chromium layer.[32] In this paper we have performed a series of implantations at a fixed implantation energy of 80 keV, varying the implantation fluence from 5×10^{16} to 1×10^{18} ions cm^{-2} (see Table 1).

RBS experiments were performed with the 5 MV HVEE Tandetron accelerator of the Centro de Micro-análisis de Materiales (CMAM) of the Universidad Autónoma de Madrid (UAM).[33] Spectra were collected using a 3.035 MeV He^+ beam, to improve the sensitivity to oxygen at the non-Rutherford cross-section resonance $^{16}O(\alpha,\alpha)^{16}O$. In order to obtain a detailed depth profile of the oxygen content in the samples, spectra were also collected using He^+ beam with higher energies ranging from 3.045 MeV to 3.105 MeV. Data were acquired simultaneously with two silicon surface barrier detectors located at scattering angles of 170° with an energy resolution of 16 keV and an ion dose of 10 μC per detector. The experimental spectra were fitted using the program RBX.[34]

Complementary to RBS, elastic recoil detection analysis (ERDA) with a time of flight (ToF) setup was performed. ERDA-ToF measurements allow a multi-element analysis, since

Table 1 Description of the coating systems studied

Sample	Implantation energy/keV	Implantation fluence/ion cm^{-2}	Thickness/nm
1	No implantation	0	95 ± 3
2	80	5×10^{16}	99 ± 3
3		1×10^{17}	109 ± 6
4		5×10^{17}	125 ± 3
5		1×10^{18}	141 ± 3

from an energy–time of flight spectrum it is possible to extract a single element spectrum. The ERDA-ToF setup is placed at the exit of the 10° beamline at the CMAM accelerator.[33] This angle has been chosen because the use of heavy ion beams at high energies requires relatively high currents in the switching magnet. The total ion current reaching the sample is measured by means of a transmission Faraday cup. The recoiled particles pass through two ToF stations,[35] and finally they impinge on a planar Si detector used for particle energy measurements. Spectra were collected using 35 MeV Au^+ incident ions up to a total dose of 20 μC.

Secondary ion mass spectrometry (SIMS) analyses have been carried out on a CAMECA Sc-Ultra instrument, employing a Cs^+ primary ion beam with an intensity of 8 nA, an impact energy of 1 keV and an incidence angle of around 60°. The secondary molecular ions MCs^+ (where M stands for O, Cr and Si) are collected from a circle area restricted to a diameter of 60 μm in the centre of a raster size of 250 μm × 250 μm. The MCs^+ mode presents reduced matrix effects, which allows analysing oxygen through the Cr/Si interface by minimising analytical artefacts.[36,37] The mass resolution $M/\Delta M$ is about 300. With these analytical conditions, the sputtering rate for Cr–Si mixed oxides is around 6×10^{-2} nm s^{-1}.

XPS spectra were measured in an ultrahigh vacuum system at a base pressure below 8×10^{-8} Pa using a hemispherical analyser (SPECS Phoibos 100 MCD-5). The pass energy was 9 eV, yielding a constant resolution of 0.9 eV. The Au $4f_{7/2}$, Ag $3d_{5/2}$ and Cu $2p_{3/2}$ lines of reference, at 84.0, 368.3 and 932.7 eV, respectively, were used to calibrate the binding energies. A twin anode (Mg and Al) X-ray source was operated at a constant power of 300 W using Mg K_α radiation. For depth profiling measurements, the ion bombardment was carried out with an angle of 45° between the normal to the sample and the ion gun using a penning ion source (SPECS IQP 10/63) with an ion beam energy of 3 keV, raising the pressure of Ar^+ to 4×10^{-2} Pa. The ion beam current density, measured with a Faraday cup that can be placed in the same position as the sample holder, was 4.6 μA cm^{-2}. The experimental conditions lead to an ion beam with a flat profile covering an area wider than 10 × 10 mm^2.

Transmission electron microscopy (TEM) studies were performed using a JEOL 3000F TEM/STEM microscope with a field-emission gun (FEG), 300 kV acceleration voltage and 0.17 nm of structural resolution. The microscope is equipped with an energy dispersive X-ray analyser unit (XEDS) and a high-angle annular dark field detector (HAADF). HAADF-STEM electrons that undergo Rutherford scattering are collected by the HAADF detector; the intensity of such images is approximately proportional to Z^2 (where Z is the atomic number of the scattering atom). The image processing of the high-resolution images was carried out using a Gatan Digital Micrograph software package. We also obtained cross-section TEM images of the sample implanted at the highest dose (1×10^{18} ions cm^{-2}). This was achieved by ion milling with a Fischione 1010 model until an electron-transparent area was obtained. The procedure is fully described in ref. 38.

Results and discussion

As stated above, prior to the experimental oxygen IBM of the Cr/Si interface, TRIDYN simulations were performed to estimate the concentration depth profiles of the elements for an implantation energy of 80 keV and ion fluences in the range of 0–1×10^{18} ions cm^{-2}. Fig. 2 shows the Cr, Si and O TRIDYN concentration depth profiles for the 80 keV oxygen IBM of a Cr(100 nm)/Si interface. It should be pointed out that the $z = 0$ coordinate in Fig. 2 indicates the instantaneous surface position, since sputtering and thin film deposition effects are included in the TRIDYN code.[25] Although fifty profiles have been calculated during each simulation for ion fluences up to 1×10^{18} ions cm^{-2}, the simulated profiles are only displayed every 1×10^{17} ions cm^{-2} for clarity purposes. The simulated profiles of Fig. 2 show that, in addition to chromium sputtering and oxygen implantation, a strong intermixing between Cr and Si is taking

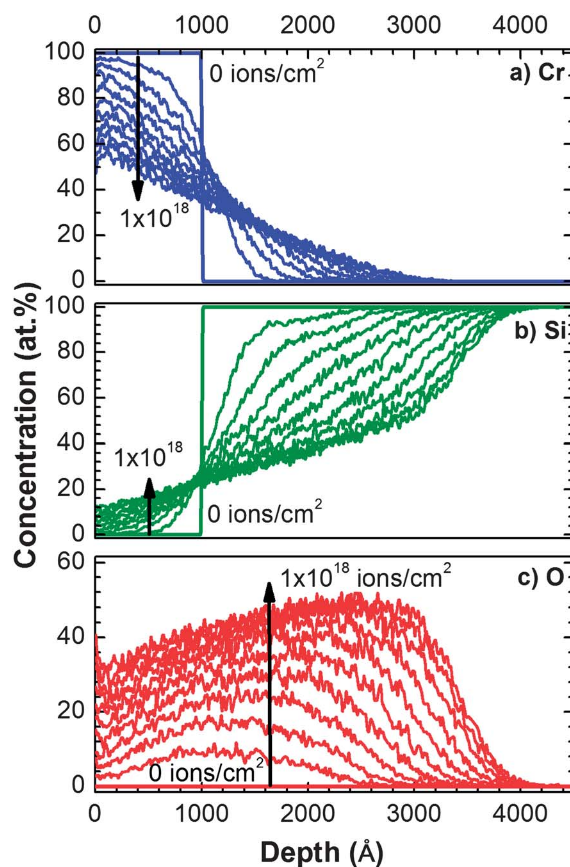

Fig. 2 Concentration depth profiles for (a) Cr, (b) Si and (c) O obtained using TRIDYN simulations for the 80 keV oxygen IBM at a Cr(100 nm)/Si interface up to ion fluences of 1×10^{18} ions cm^{-2}. Simulated profiles are displayed every 1×10^{17} ions cm^{-2}.

This journal is © The Royal Society of Chemistry 2012

place at the interface, even for low ion fluences, in such a way that the Cr/Si concentration ratio at the interface can be tailored by varying the ion dose and ion beam energy. Similar simulations were carried out for implantation energies of 40, 60 and 100 keV. It is worth to mention that the range of the oxygen implantation decreases with the ion beam energy (not shown in Fig. 2), while the apparent thickness increases with the implantation dose, therefore leading to a variation in the film thickness during IBM.

We have corroborated this increase in the film thickness by means of SEM cross-sectional measurements of the implanted samples (see Table 1). Fig. 3 shows the evolution of the layer thickness with the implantation fluence. It is evident that there is an increase in the layer thickness from the initial 95 nm up to 140 nm for the highest fluence (note that in this last result we have subtracted a 15 nm carbon contamination layer). These results follow a power law $y = a + bx^c$ with an exponent $c = 0.49$ very close to a square-root dependence typical of diffusion processes.

Fig. 4a shows the RBS profiles for the 80 keV implanted samples upon increasing the implantation fluence. The use of 3.035 MeV He^+ as incident ions provides a higher sensitivity to the oxygen content, in particular at the sample surface ($E \approx$ 1080 keV). It is evident from the raw RBS profiles that when increasing the implantation fluence two phenomena take place: (i) the amount of oxygen both at the surface and within the coatings increases (Fig. 4b) and (ii) the chromium signal progressively develops a decreasing content gradient shape together with an apparent widening of the layer thickness (Fig. 4c). The shift to lower energies in the Cr surface signal for the 1×10^{18} ions cm^{-2} is due to the presence of a surface contamination carbon layer, as we will discuss later. The RBS data can be fitted using RBX software to obtain quantified depth profiles. We present the fitted composition depth profile for the 80 keV/5×10^{17} ions cm^{-2} implanted sample in Fig. 5a. Note that the units of the depth axis are given in atoms cm^{-2}, as this is the usual nomenclature in RBS analysis. In order to convert the depth from atoms cm^{-2} to nanometre units (Fig. 5a top axis) we have to assume a density for the deposited samples. For example, we obtained a thickness of 0.8×10^{18} atoms cm^{-2} for the as-deposited sample, corresponding to 94 nm after assuming a density of 7.1 g cm^{-3} for metallic chromium,[39] in very good agreement with the layer thickness as measured by

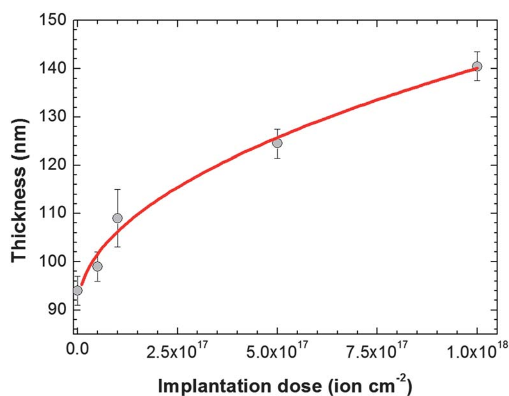

Fig. 3 Evolution of the chromium layer thickness with the oxygen implantation fluence. The solid line represents a fit of the experimental results (in circles) following a power law $y = a + bx^c$.

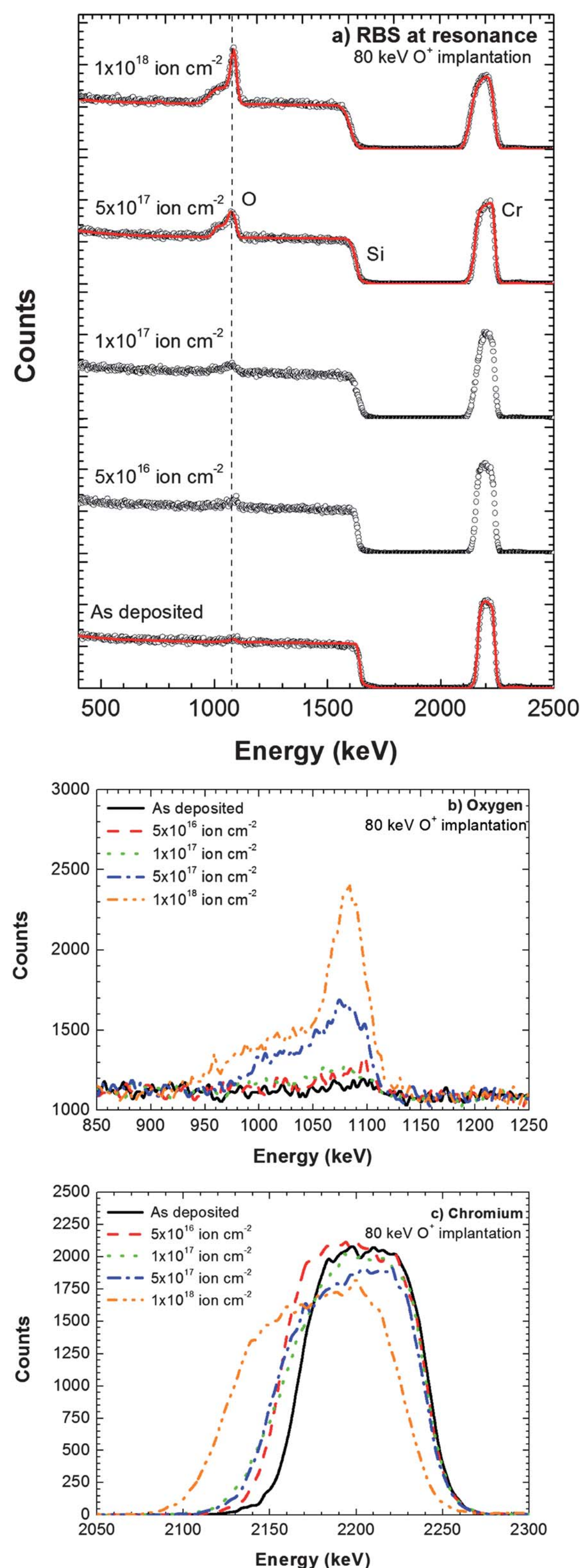

Fig. 4 (a) RBS spectra for as-deposited and oxygen implanted chromium layer on silicon performed with He^+ ions at the resonant energy of 3.035 MeV (vertical dashed line indicates the position of the surface oxygen). Solid lines represent the RBX simulation of the spectra for the as-deposited 5×10^{17} ions cm^{-2} and 1×10^{18} ions cm^{-2} samples. In (b) and (c) oxygen and chromium energy windows are plotted separately for clarity purposes.

profilometry and SEM (see Table 1). The thickness of the 5×10^{17} ions cm^{-2} implanted sample, obtained from SEM and profilometry, was 125 ± 3 nm. By using this value in the simulation procedure, we derived a density value of 6.0 g cm^{-3}, which seems a very reasonable value as it lies in between those of the metallic chromium and the Cr_2O_3 phase ($d = 5.2$ g cm^{-3}).

The composition profile is in very good agreement both qualitatively and quantitatively with the TRIDYN simulation of Fig. 5b, although the simulation predicts some silicon migration to the surface that was not observed by RBS resonant experiments. The differences in the implantation depths observed in the profiles of Fig. 5 are related to the underestimation of the sputtering made by TRIDYN.[30]

In order to improve the oxygen composition depth profile we have performed RBS experiments not only at the resonant energy of 3.035 MeV, but also at slightly higher energies (3.045–3.105 MeV), as presented in Fig. 6a for the 80 keV/1 $\times$ 10^{18} ions cm^{-2} implanted sample. By doing so, as incident He ions with $E > 3.035$ MeV will lose their energy while being implanted in the sample the resonance with oxygen atoms located deeper in the coating can be promoted. Using the stopping power of 3.1 MeV helium ions into chromium oxide calculated by SRIM,[32] we obtained an energy loss of approximately 0.30 keV per nanometre. Therefore, ions implanted at such energy will slow down to reach the resonant energy after penetrating 215 nm in the material. The selected range of implanted energies, 3.045–3.105 MeV with variations of 0.1 MeV, provides information of changes in the oxygen content every 30 nm within the layer. Furthermore, we end up with eight RBS profiles for each implantation fluence (one for each different incident energy), which allow us to have a more detailed picture of the in-depth composition, as all the data have to be fitted in RBX with the same layer structure and changing only the incident energy of the He ions. This detailed profile is shown in Fig. 6b for the 80 keV/1 $\times$ 10^{18} ions cm^{-2} implanted sample. We can now observe how, below the surface carbon contamination layer, there is a first chromium oxide layer probably due to the oxidation of the sample when exposed to the air. There is a very small amount of silicon (<1 at.%) present on the surface of the

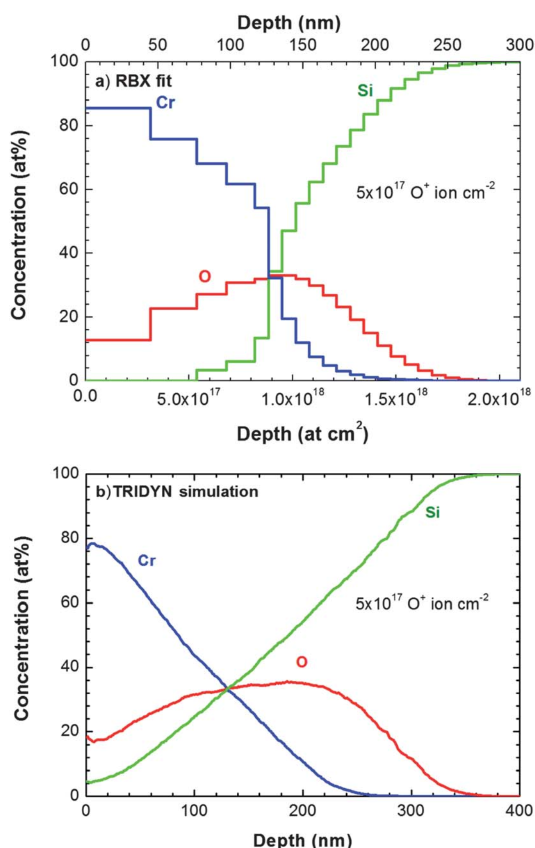

Fig. 5 Comparison of the (a) RBX fit and (b) TRIDYN simulation for the depth profile of chromium layer implanted at 5×10^{17} ions cm^{-2}.

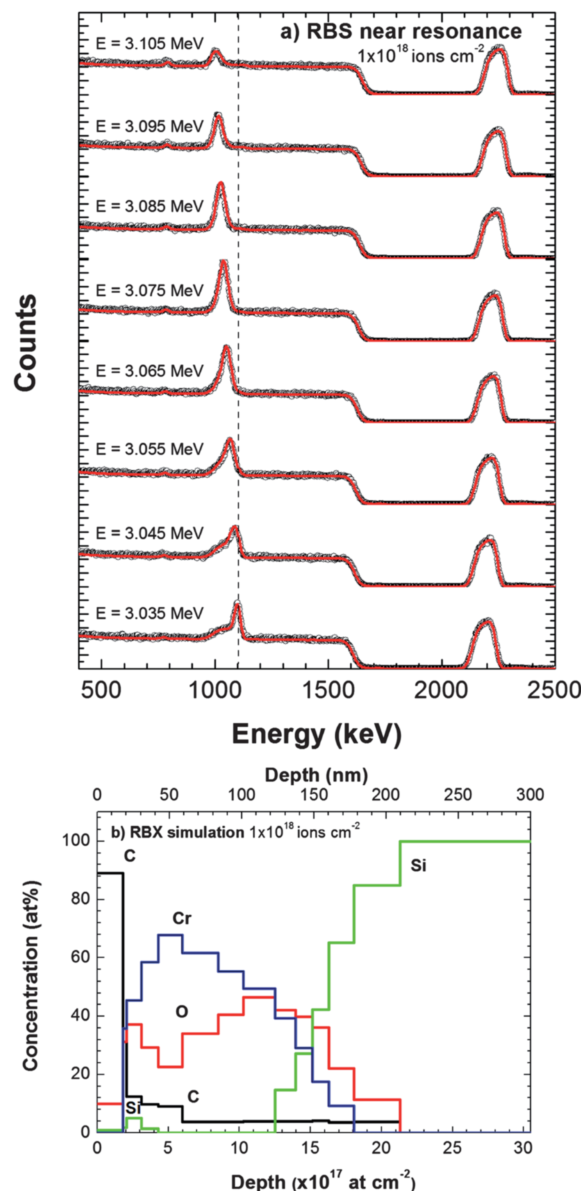

Fig. 6 (a) RBS spectra for the Cr/Si sample implanted at of 1×10^{18} ions cm^{-2}. RBS was performed with He^+ ions varying the energy from the resonant 3.035 MeV up to 3.105 MeV (vertical dashed line indicates the position of the surface oxygen). Solid lines represent the RBX simulation of the spectra for all experiments. In (b) the RBX fit of the depth profile obtained from all the experiments performed in (a).

This journal is © The Royal Society of Chemistry 2012

oxide. Despite this small concentration the presence of this element cannot be neglected, as we will prove later by SIMS and ERDA-ToF. Below this initial surface oxide layer the oxygen implantation profile is revealed. The peak of the oxygen profile is located at the chromium/silicon interface with a maximum concentration of 50 at.%, in good agreement with the TRIDYN simulations of Fig. 2. Moreover, this result indicates that the carbon contamination was produced after the oxygen implantation and, therefore, did not affect it.

The chromium profile shows an even more pronounced gradient profile than for the sample implanted at 5×10^{17} ions cm^{-2} (Fig. 5a); in this case the layer thickness increases up to 1.6×10^{18} atoms cm^{-2}, that is, twice the value as for the as-deposited sample. This change cannot be merely explained by the increase in thickness of the chromium layer from 94 to 145 nm measured by profilometry and SEM, but it also reflects a strong reduction of the density of the implanted sample. It is worth noting that the interface with the silicon substrate broadens after the highest implantation fluence, suggesting the formation of a mixed compound.

So as to complement the RBS analysis, we have performed ERDA-ToF measurements on the as-deposited and implanted samples. Fig. 7 shows the energy *vs.* time of flight plot of the (a) as-deposited and (b) 80 keV/1 $\times$ 10^{18} ions cm^{-2} implanted samples. The signals of the metallic chromium and the silicon substrate are clearly distinguished in the as-deposited sample, with very small oxygen content at the surface. On the other hand, for the sample implanted at the highest fluence, the most significant feature is the evident incorporation of oxygen into the chromium film. The tail of the oxygen signal clearly overlaps with the silicon signal, indicating the implantation of oxygen also into the substrate. In turn, the chromium signal extends toward lower energy and time of flight channels, pointing out the increase in the thickness of the chromium layer (in concordance with RBS measurements) and the formation of a ternary mixed oxide at the interface of the film. Finally, there is a clear surface layer of carbon contamination (also detected by RBS) that shifts the chromium signal towards lower energies. ERDA-ToF data consist of a two-dimensional histogram. From this two-dimensional matrix we can extract a single element contribution by selecting its corresponding hyperbolical area. The selected area can be projected in order to obtain a single element profile. Once we project the ERDA-ToF data to the energy axis we can individually compare the depth profiles of each element (Cr, Si, and O) as a function of the implanted fluence (Fig. 8). This is the main advantage of ERDA-ToF measurements as compared to RBS, where the silicon and oxygen contributions are plotted together. The elemental profiles are normalized to the total number of counts on each spectrum.

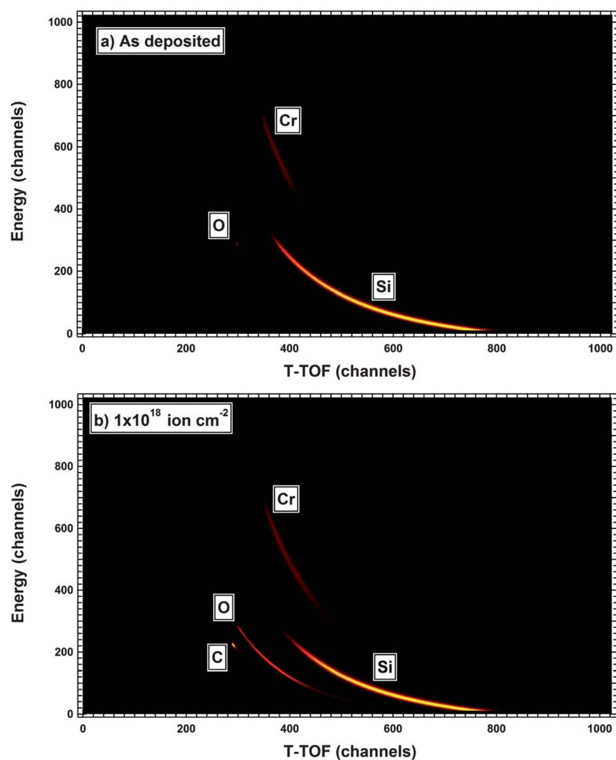

Fig. 7 ToF *versus* energy plot of the ERDA-ToF measurements for (a) as-deposited and (b) 1 $\times$ 10^{18} ions cm^{-2} oxygen implanted chromium layers obtained using a 35 MeV Au^{+} beam.

The chromium profiles (Fig. 8a) are very similar to those obtained by RBS. Hence, there is both a decrease in the signal intensity and an increase in the layer thickness upon increasing the dose. Once again, the shift in the highest fluence profile is due to the presence of a thick carbon contamination layer. This increase in the chromium layer thickness causes the shift observed in the silicon profiles (Fig. 8b). Moreover, for the two highest fluences, 5×10^{17} and 1×10^{18} ions cm^{-2}, the presence of silicon at the surface of the sample can be observed (see the inset in Fig. 8b). This result is in agreement with the TRIDYN and RBX simulations. Finally, the oxygen profiles present a double peak structure corresponding to the formation of a surface oxide and the subsequent implantation.

We have made use of the higher sensitivity of SIMS to observe physical processes that were hard to observe with the other analysis techniques, in particular for the lowest implantation fluences (see Fig. 9). If we focus on the oxygen profile evolution in function of implantation fluence (Fig. 8c), it can be clearly observed that there is a surface chromium oxide layer for all samples (first peak at extreme left of the SIMS profile). For the as-deposited reference sample, it is also possible to identify the native oxide layer of the Si wafer at a sputtering time of 2000 s. Then, for the lowest implantation fluence (5×10^{16} ions cm^{-2}), we can detect the implanted O situated at the same depth as the native Si oxide, resulting in a slightly higher O peak than for the as-deposited sample. For a higher fluence of 1×10^{17} ions cm^{-2}, a more complex O depth profile, made of three peaks, in addition to the one corresponding to the surface oxide, is observed in Fig. 9c. It can be assumed that the central peak consists of a mixed oxide $SiCr_xO_y$ with the SiO_2 native oxide included in this mixed oxide layer. It is located at longer sputtering times (*i.e.* depth) of 2300 s due to the increase in the thickness of the chromium top layer (as proved previously by RBS and ERDA experiments), owing to the oxygen insertion (and silicon to a lower extent because of the Si outward diffusion) during the implantation process. This increase in the thickness can be appreciated in the chromium and silicon profiles of Fig. 9a and b, respectively. The presence of the other two oxygen peaks (at 1800 and 2700 s, respectively) before and after the mixed oxide one

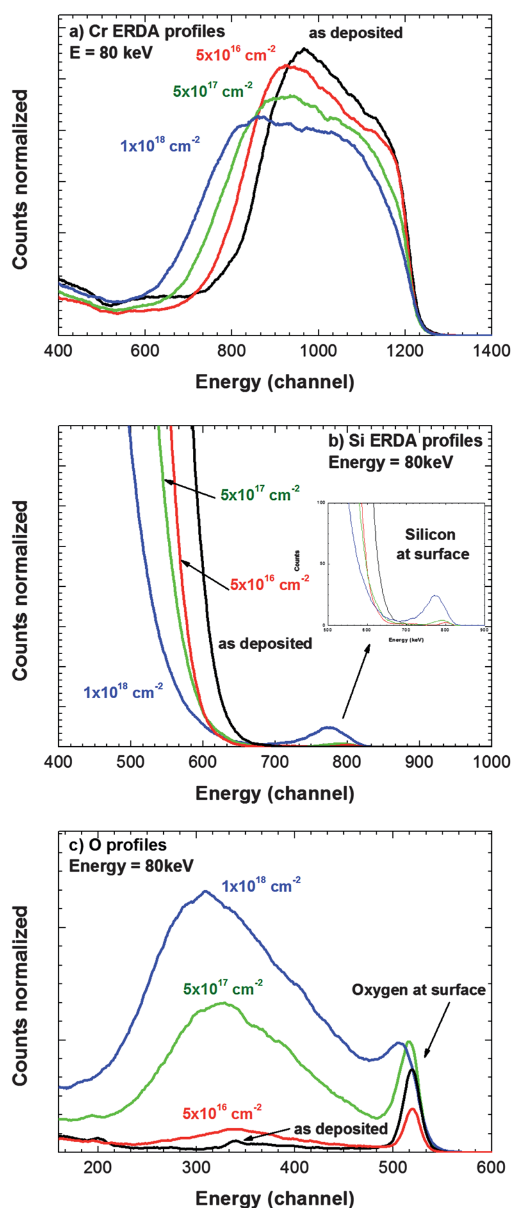

Fig. 8 Energy projections of the ERDA-ToF measurements for the as-deposited and implanted chromium layers. Energy windows of (a) chromium, (b) silicon and (c) oxygen are plotted separately for clarity purposes.

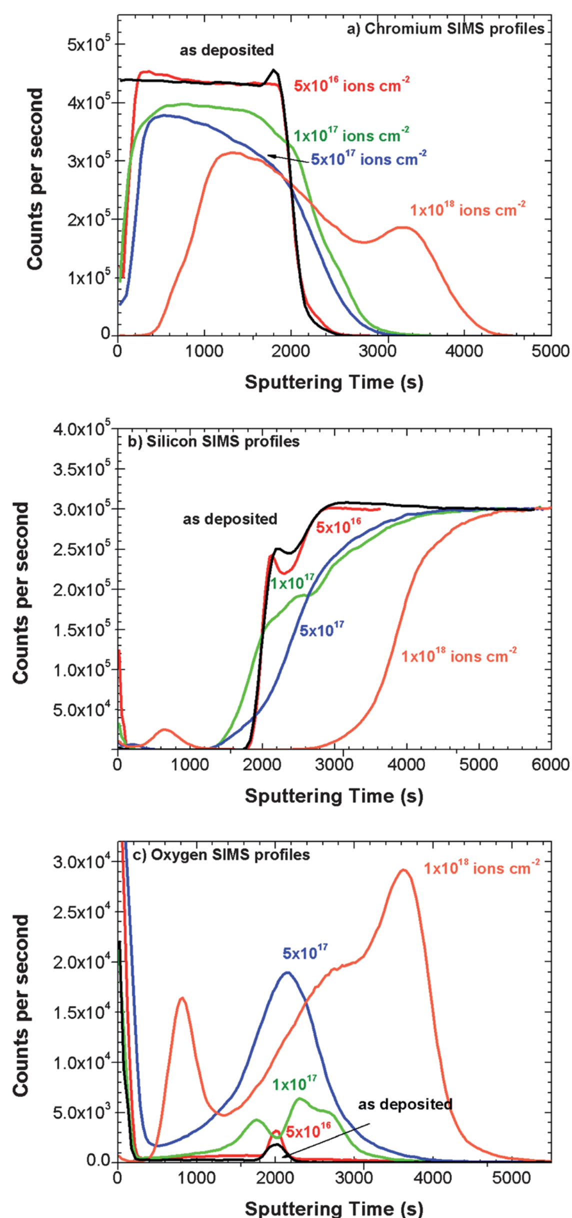

Fig. 9 SIMS elemental depth profiles for (a) chromium, (b) silicon and (c) oxygen for the as-deposited and implanted chromium layers.

together with the Cr and Si depth profiles of Fig. 9a and b may suggest the initial stages of the formation of a multi-layered oxide $CrO_x/SiCr_xO_y/SiO_x$ confirmed by TEM for higher implantation fluences (see below). The formation of this multilayer can only be observed with the high depth resolution of SIMS for low implantation fluences. In this case, the Cr/Si interface becomes less abrupt as the implantation of oxygen initiates the mixing mechanism. Then, at 5×10^{17} ions cm^{-2}, a single and intense O peak at the interface is observed in Fig. 9c, together with a very gradual variation of the Cr and Si profiles (Fig. 9a and b). This could be related to the formation of a larger mixed Cr–Si–O oxide layer between Cr and Si or a mixing of CrO_x and SiO_x phases. Moreover, it is possible to detect the presence of a Si-doped chromium oxide layer at the surface (see Fig. 9b) owing to outward diffusion of silicon, enhanced by ion implantation, as had already been observed with RBS and ERDA-ToF. Finally, for the highest fluence of 1×10^{18} ions cm^{-2}, the shift in the chromium, silicon and oxygen profiles due to the presence of a carbon contamination surface layer produced after the implantation process can be clearly observed. SIMS has allowed us to resolve better the thicker chromium oxide formed at the surface of the coating after the highest implantation fluence. The outward diffusion of Si is much more visible at this fluence, suggesting the formation of a Si-doped chromium oxide top layer richer in Si. Below this surface oxide there is still a layer of metallic chromium doped with O for this high implantation fluence (corroborated by XPS, as will be discussed later). This metallic region becomes thinner when increasing the implantation fluence. Therefore, it is clear that a much higher dose is

This journal is © The Royal Society of Chemistry 2012

needed to transform completely the metallic Cr layer into a homogeneous Cr oxide layer by oxygen implantation. Below the Cr layer, there is a broad O peak corresponding to a CrO_x layer, followed by a more intense peak sited deeper in the sample, probably corresponding to a Si-doped CrO_x with a higher content of chromium compared with silicon. This third peak is accompanied by an increase in the chromium signal (Fig. 9a) and is related to the formation of small $SiCrO_x$ "bubbles" below the interface as observed by TEM (see below).

More experiments are needed to understand better these processes. For example, for low implantation fluences, the use of ^{18}O isotopic tracer for implantation would allow an even better understanding of the implantation process by allowing a separation between the native oxide present in silicon and the implantation induced oxide.

Fig. 10 a–d show the typical XPS concentration depth profiles (CDP) of the 95 nm thick chromium film after O^+ implantation at 80 keV at different ion fluences from 5×10^{16} to 1×10^{18} ions cm^{-2} using Ar^+ ion bombardment at 3 keV and at an angle of incidence of 45°. The carbon, chromium, oxygen and silicon concentrations have been plotted as a function of depth. To carry out this task, the C1s, Cr2p, O1s and Si2p intensities (band areas), after background subtraction using the Shirley method,[40] were used to calculate the concentration using the following eqn (1):

$$C_x = \frac{I_x/S_x}{\sum_i I_i/S_i} \quad (1)$$

where C_x is the atomic concentration of element x, assumed to be uniform on the surface, I_x is the measured intensity for this element and S_x its sensitivity factor provided by the manufacturer ($S_C = 1$, $S_{Cr} = 11.5$, $S_O = 2.85$, $S_{Si} = 0.865$). Since intensities are measured as a function of the erosion time, the erosion rate measured on the 95 nm thick chromium film of ~0.37 nm min^{-1} was used as a reference to calibrate the depth scale. This approximation seems to be plausible, as the observed increase in the thickness of the coating with the implantation, from 95 up to 150 nm, is in perfect agreement with the profilometry and SEM measurements (see Table 1).

As can be observed in the CDP of Fig. 10, the ion fluence is a critical parameter for the result of the O^+ implantation. For the lowest ion fluence of 5×10^{16} ions cm^{-2} (Fig. 10a), despite the surface oxidation of the chromium layer, the small quantity of oxygen detected in the coating (<3 at.%) was not bonded to the metals, but was more likely to be dissolved in the film. A similar result was obtained for the samples implanted at 1×10^{17} ions cm^{-2} (Fig. 10b); that is, the chromium layer remains as metallic chromium with some oxygen being dissolved (6 at.%). However, there is a non-negligible increase in the oxygen content at the Cr/Si interface that indicates the initial stage of the formation of oxides, as previously suggested by SIMS. Furthermore, with increasing oxygen dose (Fig. 10c and d), oxygen incorporates within the film framework, leading to a strong chemical reaction and IBM at the Cr/Si interface. In particular, for the highest fluence of 1×10^{18} ions cm^{-2}, the formation of a chromium surface oxide of approximately 25 nm followed by a metallic chromium layer and an oxide multilayer structure is evident. At the maximum of the oxygen profile, the formation of Cr–O bonds was detected, while Si–O bonds were found at the interface with the silicon substrate.

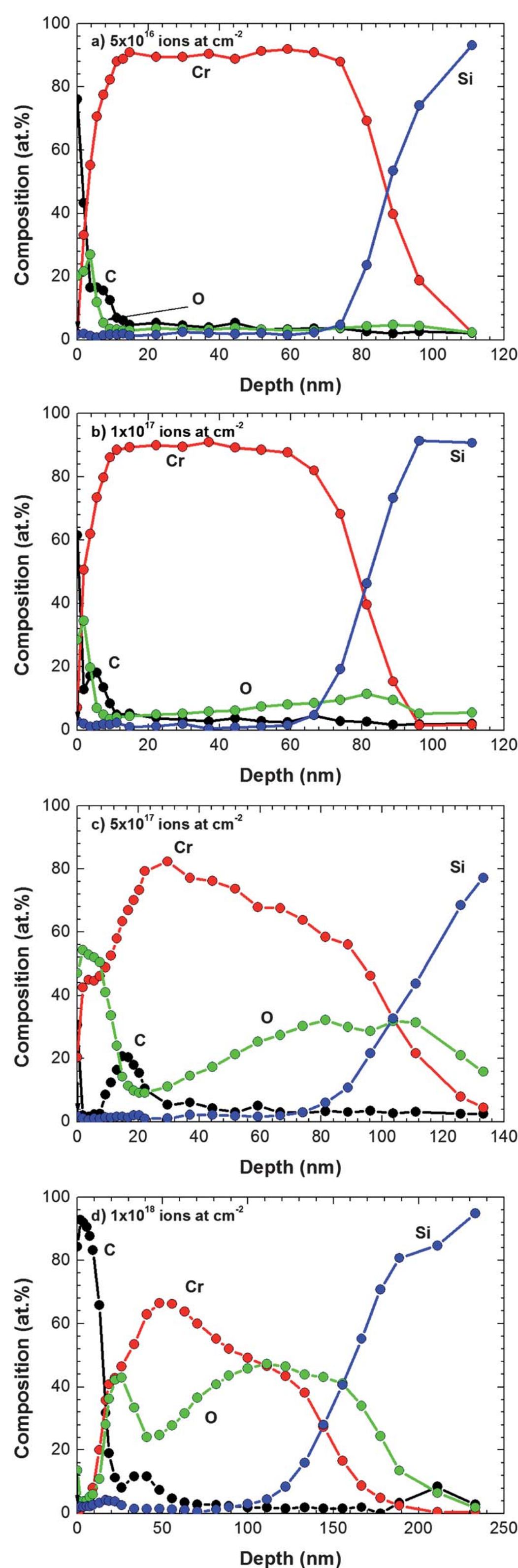

Fig. 10 XPS depth profile for chromium layer oxygen implanted with (a) 5×10^{16}, (b) 1×10^{17}, (c) 5×10^{17} and (d) 1×10^{18} ions cm^{-2}.

Since no clear evidence of the formation of a Cr–O–Si mixed oxide has been found, additional experiments have to be carried out to elucidate this point. For the highest fluence, the presence of silicon

This journal is © The Royal Society of Chemistry 2012

at the surface of the chromium layer can be detected, in fair agreement with previously reported experiments by RBS, ERDA and SIMS. It should be pointed out that the maxima of oxygen distributions fairly agree with the ion ranges calculated from SRIM simulations at 80 keV. Finally, as observed in Fig. 10 the C distribution is not homogeneous along the oxide film. Two layers are observed; the outer layer is attributed to a graphite-like contamination layer and is attributed to the sample exposure to the atmosphere during manipulation from the preparation chamber to the analysis chamber. The inner one is produced during implantation (since implantation uses CO_2 as precursor gas). Carbon species related to this layer are associated with a C1s band at ~2.5 eV below the band associated with the graphitic layer as measured by XPS (not shown here) and is currently explained as due to carbide species.

It is worth noting that angle-resolved XPS measurements (ARXPS) carried out at different points of the CDP (not shown) did not display changes either in the Cr concentration or in the O concentration, therefore indicating the absence of compositional changes within the depth probed by ARXPS. These results allow ruling out oxygen preferential sputtering during depth profiling.

Despite the differences in principles and bases for all the depth profile techniques used in this work, the comparison among the results obtained using each of them allows gaining a thorough knowledge into the characteristics of the mixed oxides. We have plotted the oxygen depth profiles obtained from RBS, ERDA-ToF, SIMS and XPS for the sample implanted at 1×10^{18} ions cm^{-2} in Fig. 11. For RBS and XPS, quantitative profiles of concentration *versus* depth can be straightforwardly obtained as previously described. In order to compare the qualitative ERDA-ToF and SIMS profiles with the quantitative XPS and RBS profiles, we have applied conversion factors to the energy (and time) and the normalized counts so as to match the position and concentration of the maxima of the oxygen profile. No further handling of the profiles was performed; therefore, we can conclude that they are in excellent agreement. The different degree of sensitivity of the depth profiling techniques used in this study pointed out the complexity of the diffusion processes and oxide layer formations induced by the ion implantation as a function of the dose. Although ion implantation is carried out at room temperature and the radiation-induced defects have limited mobility, due to the high ion dose used, their concentrations can exceed to a great extent the thermodynamic equilibrium values leading to an increase of the diffusion coefficients.[41] Therefore, in our case, the changes in subsurface composition during ion bombardment should be attributed to radiation-induced diffusion mechanisms. We have determined that the more homogeneous mixed oxide layer is formed for fluences higher than 5×10^{17} ions cm^{-2}. For lower fluences, thicker CrO_x and SiO_x layers are formed compared with the mixed oxide layer. In the light of these results, it is clear that either higher implantation doses or a post-implantation annealing treatment would be required to obtain more stoichiometric and homogeneous oxide films as the ones prepared with reactive magnetron sputtering.[13,14]

Finally, we have compared the results obtained for the different depth profiling analyses with the observations made by TEM on the sample implanted at 1×10^{18} ions cm^{-2}. The inset of Fig. 12 shows a bright field image of a cross-section of the analysed sample. From left to right we can observe: (1) a darker zone of approximately 100 nm, labelled Cr(O) because the main elements present were chromium and oxygen, according to XEDS analysis; (2) a lighter zone of ~100 nm, named Si(O) and (3) the crystalline silicon substrate, labelled Si. The Cr(O) layer has an irregular contrast and is markedly wavy, probably owing to the O^+ implantation. The Si(O) layer has also a thickness of ~100 nm, corresponding to the implantation range of the oxygen ions, which indicates that this layer has been formed during the implantation process. In the enlarged corresponding STEM-HAADF image of Fig. 12 the previously described zones are seen in more detail. It is worthy to note that in this picture the contrast is approximately proportional to Z^2 (Z being the atomic number), that is, a brighter contrast corresponds to an element with a higher Z. In the aforementioned 100 nm Cr(O) zone, we

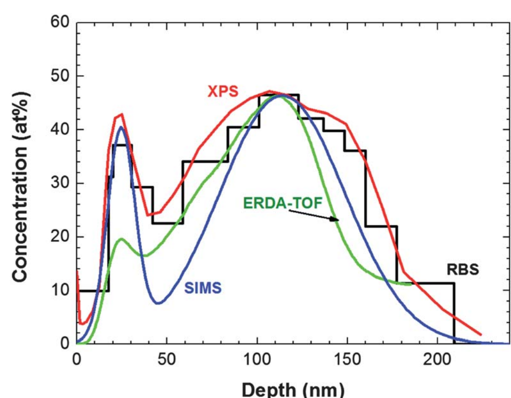

Fig. 11 Comparative depth profiles obtained by RBS, ERDA-ToF, XPS and SIMS for chromium sample oxygen implanted at 1×10^{18} ions cm^{-2}.

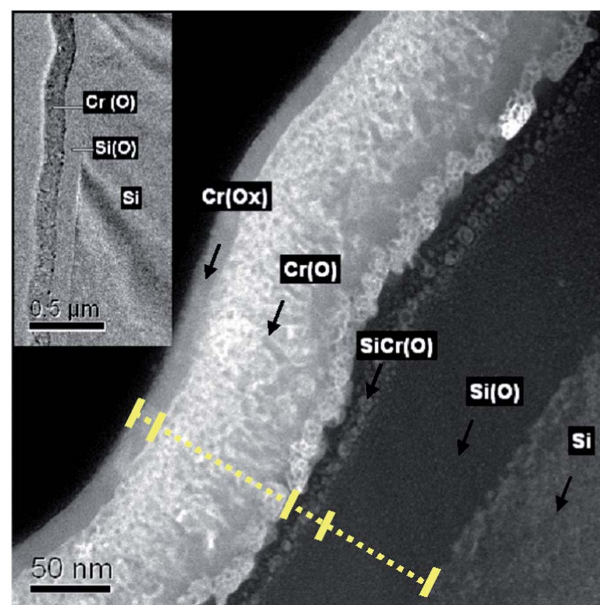

Fig. 12 Cross-sectional STEM-HAADF image of the 1×10^{18} ions cm^{-2} sample. Labels on the different areas indicate the main elements present according to STEM-XEDS analysis. The discontinued line marks the position in which a XEDS line scan has been made. The inset corresponds to a bright field larger area of the sample.

This journal is © The Royal Society of Chemistry 2012

can now distinguish a surface layer with a thickness of 15–20 nm. This layer has been labelled as $Cr(O_x)$ because its contrast implies that the amount of oxygen present in the layer is higher than in the subsequent Cr(O) zone. Therefore, it is related to a more oxidized phase, as confirmed by XEDS–STEM analysis. The chromium oxide in this zone corresponds to the amorphous oxide layer that was observed in all the depth profiles (see Fig. 11). The following Cr(O) zone has an irregular contrast and a thickness of about 100 nm, corresponding to the thickness of the as-deposited chromium layer. Although the Cr oxidation state cannot be determined by TEM, the contrast suggests a lower oxidation state as compared to the top oxide layer. The mean contrast is brighter than for the $Cr(O_x)$ layer, which indicates the predominance of chromium with a lower amount of oxygen, as corroborated by STEM-XEDS. Contrast variation along this zone can be attributed to a non-homogeneous distribution of the oxygen leading to crystalline aggregates of chromium oxides. More experiments are in progress in order to determine structural characteristics of the aggregates.

The next bright contrast observed in Fig. 12 is very interesting. It is formed by crystalline bubble-like structures composed of chromium, silicon and oxygen as deduced from XEDS. This zone has been labelled SiCr(O) and it continuously extends parallel to the Cr(O) layer. The presence of both silicon and oxygen (both with a lower Z than of chromium) in this fringe is responsible for the darker contrast observed in the bubbles in relation with the Cr(O) layer. This zone, about 15–30 nm wide, is less wavy than the previous ones; it corresponds to the increase in the chromium signal observed in the depth profiles (see, for example, the SIMS chromium profile of Fig. 9a) for the highest implantation fluence. After this zone, only silicon and oxygen are observed. The Si(O) layer has an almost constant thickness of 90 nm and it goes parallel to the silicon substrate without any waving appearance. As stated above, the formation of this amorphous silicon–oxygen layer is attributed to the implantation procedure. The interface of this amorphous layer with the crystalline silicon is not flat, showing a certain roughness, and defects such as dislocations can be seen in the bright field high resolution images (not shown here).

Fig. 13 shows the elemental depth profile obtained in a STEM-XEDS linescan across the TEM cross-section (see dashed line in Fig. 12). In the marked line, the depth measurements are 17 nm for $Cr(O_x)$, 100 nm for Cr(O), 25 nm for SiCr(O) and about 75 nm for the Si(O) layer. In this depth profile, the surface contamination carbon layer observed in the RBS, SIMS, ERDA and XPS profiles cannot be unambiguously distinguished since a carbon containing glue was used during the preparation of the cross-section samples for TEM examination. Therefore, in Fig. 13 we have placed the surface of the sample (depth = 0 nm) at the position where the chromium signal is first detected. The chromium line extends approximately up to 140–150 nm, that is, exactly to where the bubbles end. The small peak at this position clearly indicates the presence of chromium in these aggregates. The disappearance of the Cr signal after 150 nm discards the presence of chromium (either on a binary or a mixed oxide form) in the darker Si(O) zone of Fig. 12. This line corresponds well with the depth profile as measured by XPS, SIMS, RBS and ERDA. The amount of oxygen remains constant within these 150 nm, with a subsequent decrease down to a new constant value until reaching the silicon substrate. This result allows to suppose that the zone labelled as Si(O) is either SiO_2 or SiO_x (with $x < 2$). With respect to the silicon, there is a clear progressive penetration of silicon atoms in the original chromium layer but no evidence of silicon surface segregation was found. Therefore, the TEM observations do not allow discarding the formation of a crystalline mixed Cr–Si oxide in the bubbles zone. Fourier transforms performed in these rounded crystalline areas will give interesting information about this point, and so further work is being carried out in this direction.

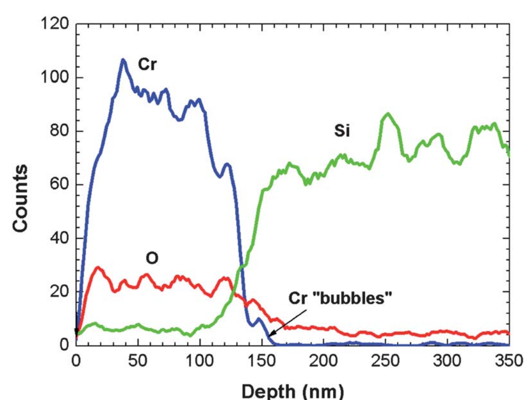

Fig. 13 Elemental depth profile obtained by the STEM–XEDS line scan across the yellow discontinued line marked in Fig. 12. In that position measurements of the different zones are: 17 nm for $Cr(O_x)$, 100 nm for Cr(O), 25 nm for SiCr(O) and about 75 nm for the Si(O) layer.

In summary, it is clear that a complete picture of the implanted samples depth profiles cannot be obtained without the combined characterisation approach applied in this work. The oxygen-resonant RBS experiments provide an unambiguous description of the oxygen depth profiles together with an estimation of the density changes upon implantation. The element separation in the ERDA-ToF profiles allows the observation of subtle phenomena such as the silicon surface segregation of doses higher than 5×10^{17} ions cm^{-2}. This effect was confirmed by the high element sensitivity of SIMS, which equally elucidates the initial stages of the mixed oxide formation at the chromium/silicon interface. The XPS depth profiles confirmed all these results, and provide information regarding the chemical bonding of the elements (*i.e.* the formation of Cr–O bonds or the appearance of carbides species). The depth profile information obtained by four different spectroscopic techniques has been corroborated by cross-sectional STEM measurements.

Conclusions

The formation of chromium–silicon mixed oxide thin films by oxygen ion implantation of metallic Cr thin films deposited by magnetron sputtering on Si substrates has been studied. We have performed an extensive depth profiling characterization of the films as a function of the implantation fluence by means of RBS, ERDA-ToF, SIMS and XPS. This comparative multi-technique depth profiling analysis converges to assess an increase in the chromium layer thickness and a broadening of the chromium/silicon interface with increasing the implantation fluence. This behaviour suggests, that for the experimental conditions used,

the oxygen implantation rate is higher than the Cr and Si sputtering removal rates, therefore leading to the thin film deposition regime, in such a way that the distance between the original Cr/Si interface and the surface increases with the ion fluence, in agreement with the TRIDYN results. The results suggest the formation of a ternary mixed compound at the interface. However, oxygen fluences higher than 1×10^{18} ions cm^{-2} are needed, not only to elucidate this point, but also to transform completely the metallic chromium layer into chromium oxide layer by oxygen implantation. There is also evidence of silicon segregation at the surface of the films for fluences higher than 5×10^{17} ions cm^{-2}. The agreement both qualitatively and quantitatively (in depth) of the TEM cross-sectional measurements and the depth profile obtained by the rest of analytical spectroscopies is highly remarkable. These changes are expected to be reflected in a controlled variation of the optical properties of the films, in particular in the refraction index.

Acknowledgements

This work was financially supported by the Spanish Ministerio de Ciencia e Innovación (projects MAT2008-06618-C02 and FUNCOAT-CSD2008-00023). REG would also like to thank the MCINN for the financial support within the Ramón y Cajal programme. AIN acknowledges the financial support of the Region of Navarra. Likewise, the authors gratefully acknowledge Mr A. Medrano (AIN) for carrying out the oxygen implantations, Mr E. Urones (I.C.T.S. Centro Nacional de Microscopía Avanzada, UCM) for the TEM assistance, the personnel from the Servicio de Microscopía (ICMM-CSIC) for the preparation of cross-sectional samples for TEM and Dr M. Posselt (Institute of Ion Beam Physics and Materials Research, Forschungszentrum Rossendorf, Dresden, Germany) for licensing the use of TRIDYN program.

Notes and references

1 S. Qiu and T. L. Starr, *J. Electrochem. Soc.*, 2007, **154**(6), H472.
2 M. Hirano, C. Nakahara, K. Ota and M. Inagaki, *J. Am. Ceram. Soc.*, 2002, **85**(5), 1333.
3 V. Stengl and S. Bakardjieva, *J. Phys. Chem. C*, 2010, **114**, 19308.
4 C. Wang, B. Q. Xu, X. Wang and J. Zhao, *J. Solid State Chem.*, 2005, **178**, 3500.
5 A. Kubacka, M. Fernández-García and G. Colón, *J. Catal.*, 2008, **254**, 272.
6 H. Kang, M. Heo and H. Sohn, *Curr. Appl. Phys.*, 2010, **10**, 22.
7 J. Yan, Y. Kuo and J. Lu, *Electrochem. Solid-State Lett.*, 2007, **10**(7), H199.
8 F. Gracia, F. Yubero, J. P. Holgado, J. P. Espinos, A. R. González-Elipe and T. Girardeau, *Thin Solid Films*, 2006, **500**, 19.
9 S. Lisinski, J. Krause, D. Schaniel, L. Ratke and T. Woike, *Scr. Mater.*, 2008, **58**, 553.
10 G. Frenzer and W. F. Maier, *Annu. Rev. Mater. Res.*, 2006, **36**, 281.
11 F. Hamelmann, K. Gesheva, T. Ivanova, A. Szekeres, M. Abrashev, U. Heinzmann and J. Optoelectron, *Adv. Mater.*, 2005, **7**, 393.
12 E. Avendaño, A. Azens, G. A. Niklasson and C. G. Granqvist, *J. Solid State Electrochem.*, 2003, **8**, 37.
13 L. Vergara, R. Escobar Galindo, R. Martínez, O. Sánchez, C. Palacio and J. M. Albella, *Thin Solid Films*, 2011, **519**, 3509.
14 N. Benito, D. Díaz, L. Vergara, R. Escobar Galindo, O. Sánchez and C. Palacio, *Surf. Coat. Technol.*, 2011, **206**, 1484–1489.
15 M. Nastasi and J. W. Mayer, *Mater. Sci. Eng., R*, 1994, **12**, 1.
16 C. Palacio and A. Arranz, *Surf. Sci.*, 2005, **578**(1–3), 71.
17 C. Palacio and A. Arranz, *J. Phys. D: Appl. Phys.*, 2008, **41**, 035301.
18 A. Arranz and C. Palacio, *Thin Solid Films*, 2007, **515**(7–8), 3426.
19 C. Palacio and A. Arranz, *Surf. Sci.*, 2006, **600**, 2385.
20 A. Arranz and C. Palacio, *Surf. Sci.*, 2007, **601**(18), 4510.
21 Y. Okabe, M. Iwaki and K. Takahashi, *Mater. Sci. Eng., A*, 1989, **115**, 79.
22 Y. Bohne, N. Shevchenko, F. Prokert, J. von Borany, B. Rauschenbach and W. Möller, *Vacuum*, 2004, **76**, 281.
23 V. Singh, A. D. Yadav, S. K. Dubey, B. K. Panigrahi and B. M. Arora, *Surf. Coat. Technol.*, 2009, **203**(17–18), 2632.
24 W. Möller and W. Eckstein, *Nucl. Instrum. Methods Phys. Res., Sect. B*, 1984, **2**, 814.
25 W. Möller, W. Eckstein and J. P. Biersack, *Comput. Phys. Commun.*, 1988, **51**, 355.
26 W. Eckstein, Computer Simulationof Ion-Solid Interactions, in *Springer Series in Materials Science*, Springer-Verlag, vol. 10, 1991.
27 W. D. Wilson, L. G. Haggmark and J. P. Biersack, *Phys. Rev. B: Solid State*, 1977, **15**, 2458.
28 J. Lindhard and M. Scharff, *Phys. Rev.*, 1961, **124**, 128.
29 O. S. Oen and M. T. Robinson, *Nucl. Instrum. Methods*, 1976, **132**, 647.
30 W. Möller and M. Posselt, *TRIDYN User Manual, Institute of Ion Beam Physics and Materials Research*, Forschungszentrum Rossendorf, http://www.hzdr.de/FWI/FWIT/FILES/Manual_TRIDYN_FZR.pdf.
31 R. Martınez, J. A. Garcıa, R. J. Rodrguez, B. Lerga, C. Labrugere, M. Lahaye and A. Guette, *Surf. Coat. Technol.*, 2003, **174–175**, 1253.
32 J. F. Ziegler, M. D. Ziegler and J. P. Biersack, *Nucl. Instrum. Methods Phys. Res., Sect. B*, 2010, **11–12**, 1818.
33 A. Climent-Font, F. Pászti, G. García, M. T. Fernández-Jiménez and F. Agulló, *Nucl. Instrum. Methods Phys. Res., Sect. B*, 2004, **219–220**, 400.
34 E. Kotai, *Nucl. Instrum. Methods Phys. Res., Sect. B*, 1994, **85**, 588.
35 S. Giangrandi, T. Sajavaara, B. Brijs, K. Arstila, A. Vantomme and W. Vandervorst, *Nucl. Instrum. Methods Phys. Res., Sect. B*, 2008, **266**(24), 5144.
36 Y. Gao, Y. Marie, F. Saldi and H.-N. Megion, *Int. J. Mass Spectrom. Ion Processes*, 1995, **143**, 11.
37 F. Wu, N. Valle, R. Fitzpatrick, J. G. Ekerdt, L. Houssiau and H. N. Migeon, *Surf. Interface Anal.*, 2011, **43**(1–2), 669.
38 M. Manso-Silván, M. Langlet, J. M. Martínez-Duart and P. Herrero, *Nucl. Instrum. Methods Phys. Res., Sect. B*, 2007, **257**, 623.
39 http://www.webelements.com/chromium/physics.html.
40 D. A. Shirley, *Phys. Rev. B: Condens. Matter*, 1972, **5**, 4709.
41 N. Q. Lam, *Surf. Interface Anal.*, 1988, **12**, 65.

This journal is © The Royal Society of Chemistry 2012